## PAPER

Check for updates

# A truncated octahedron NaCe(MoO$_4$)$_2$ nanostructure: a potential material for blue emission and acetone sensing†

Nibedita Haldar,‡[a] Tanmoy Mondal,[a] Tanushri Das,[ab] Debabrata Sarkar,[c] Mrinal Pal,[b] Asiful H. Seikh[d] and Chandan Kumar Ghosh [ID] *[a]

Scheelite-type NaCe(MoO$_4$)$_2$, a promising nanostructure for optoelectronic applications, has been synthesized using a typical hydrothermal technique, and its structural and microstructural properties have been characterized using several microscopic and spectroscopic techniques. We observed intense blue emission from the 5d–4f transitions of Ce$^{3+}$ within CeO$_8$, while the presence of mono-(CeO$_7$) and divacancies (CeO$_6$) of oxygen cause relatively weak emissions at 488 nm, 462 nm and 531 nm. Our study reveals that the use of trisodium citrate during synthesis plays a significant role to tune the formation of CeO$_7$ and CeO$_6$, which in consequence also modify the band edges of the system. The Commission Internationale de l'Eclairage (CIE) coordinates are found to be within the blue region with a correlated color temperature (CCT) of ∼7854 K, indicating the potential of NaCe(MoO$_4$)$_2$ nanostructures for cold solid-state lighting applications. Moreover, the oxygen deficiencies are found to act as active sites for the selective adsorption of acetone, leading to acetone sensing. Hence, NaCe(MoO$_4$)$_2$ nanostructures may be potential smart materials for blue-lighting and acetone sensors. *Ab initio* calculations have been carried out to obtain theoretical insights into the electronic structure of the bare and oxygen-deficient NaCe(MoO$_4$)$_2$ and to understand the guiding parameters for acetone sensing. Our calculations also demonstrate that acetone adsorption occurs mostly through the (112) plane.

## 1. Introduction

Recently, rare-earth (RE)-based scheelite micro/nanostructures have attracted considerable interest from researchers for various optoelectronic applications, including solid-state lasers, fluorescent lamps, optical sensors, scintillators, light-emitting diodes, fiber optic communications, and biological labeling due to their unique features of tuneable emission, narrow bandgap, high quantum yield and high opto-electric conversion, and excellent thermal and chemical stability.[1–3] Among them are the alkali RE binary molybdates with the generic formula A$^I$Ln$^{III}$(MoO$_4$)$_2$ (A = alkali metal, Ln = RE lanthanide), in which the Ln$^{3+}$ embedded in the A$^+$ lattice exhibits a strong 5d–4f transition depending on the symmetry of the unit cell.[4,5] Extensive research work has been carried out by various researchers, including us, to understand the parameters influencing the emission. As an example, Cheng *et al.* have investigated the influence of Li/Ag on the luminescence properties of Li$_{1-x}$Ag$_x$Lu(MoO$_4$)$_2$:Eu$^{3+}$,[6] while Song *et al.* have explored red emission from Eu$^{3+}$-doped AgGd(MoO$_4$)$_2$.[7] The strong integrated emission and higher color purity observed for LiEu(MoO$_4$)$_2$ among the AEu(MoO$_4$)$_2$ materials (A = Li$^+$, Na$^+$ and K$^+$) have been ascribed to its higher, faster charge transfer due to the shortened and more covalent Li–O bond in comparison with those of its Na or K counterpart.[8] Most of the conventional techniques (*e.g.*, the Czochralski method, solid-state reaction, *etc.*) lead to agglomeration with high grain size and irregular morphology;[9] however, recent studies reveal a remarkable correlation between the morphology and emission as the selection rules of optical transition significantly depend on shape, size, exposure facets, dimensionality, hierarchy, *etc.* To date, abundant efforts have been devoted to generating various scheelite micro/nanostructures using hydrothermal and other techniques to gain an intuitive understanding of

[a] *School of Materials Science and Nanotechnology, Jadavpur University, Jadavpur, Kolkata-700032, India. E-mail: chandan.kghosh@jadavpuruniversity.in; Tel: +91 033-2457-3028*

[b] *CSIR-Central Glass and Ceramic Research Institute, Kolkata-700032, India*

[c] *Applied NanoPhysics Laboratory, Department of Physics and Nanotechnology, SRM Institute of Science and Technology, Kattankulathur-603203, India*

[d] *Mechanical Engineering Department, College of Engineering, King Saud University, Riyadh, 11421, Saudi Arabia*

† Electronic supplementary information (ESI) available. See DOI: https://doi.org/10.1039/d4ma00306c

‡ At present: University of Engineering and Management, New Town, Kolkata-700160, India.

optical emissions. As a reference, Liu *et al.* reported the preparation of uniform tetragonal microspindles and nanoplates using the surfactant ethylenediaminetetraacetic acid (EDTA-2Na),[10] while microrods, microcuboids and microflowers have been obtained *via* a synthesis technique based on the ligand polyvinylpyrrolidone.[11] Zheng *et al.* synthesized a cotton-shaped 3D flower-like morphology using a trisodium citrate assisted method,[12] whilst uniform spherical nanoparticles have been achieved *via* a cetyltrimethyl ammonium bromide (CTAB) assisted hydrothermal method.[13] A triclinic → tetragonal phase transition was observed by our group during the CTAB-assisted hydrothermal synthesis of $NaCe(WO_4)_2$.[14,15]

In this manuscript, we report for the first time a $NaCe(MoO_4)_2$ truncated octahedral nanostructure with inherent oxygen mono- and divacancy ($V_O$ and $2V_O$) defects and describe the role of these defects in its photoluminescence. In addition, $V_O$ and $2V_O$ often accumulate at the surface of nanostructures and trap electrons that facilitate gas-sensing properties.[16–19] Although optical studies have been reported in the literature, reports on the gas-sensing of scheelite nano/microstructures are very rare. As an example, Lin *et al.* reported the $V_O$-induced gas sensing activity of $NaBi(MoO_4)_2$ nanomaterials,[20] while our recent study demonstrated the $NH_3$-sensing ability of $NaCe(WO_4)_2$.[14] We herein also identify acetone-sensing ability in $NaCe(MoO_4)_2$ nanostructures, with $V_O$ and $2V_O$ playing crucial roles in determining the sensitivity. To the best of our knowledge, this is the first report on the acetone-sensing ability of $NaCe(MoO_4)_2$. Additionally, as there have been no in-depth theoretical calculations on the electronic structure of $NaCe(MoO_4)_2$, to achieve a better understanding, we have also calculated the *ab initio* band structure of $NaCe(MoO_4)_2$. The calculations reveal that the Ce $5d_{z^2}$, $d_{x^2-y^2}$, and $d_{yz}$ orbitals result in blue and green emissions in the presence of $V_O$ and $2V_O$, respectively. We have demonstrated that the electronic excitation involved the $MoO_4$ tetrahedra and that emission takes place within the $CeO_8$ polyhedra, while $MoO_4 \rightarrow CeO_8$ charge transfer is mediated through the $\nu_4(F_2)$ phonon mode. Overall, it may be inferred that the truncated octahedron $NaCe(MoO_4)_2$ nanostructures have strong potential in violet emission and sensing applications.

# 2. Experimental section

## 2.1 Materials and synthesis

To prepare $NaCe(MoO_4)_2$ nanomaterials through the typical hydrothermal method, 1.00 mmol (0.434 g) of cerium nitrate [$Ce(NO_3)_3 \cdot 6H_2O$, Merck, Germany] and trisodium citrate [$Na_3Cit \cdot 2H_2O$, Merck, Germany] were mixed with 60 ml DI water, followed by stirring for 2 h at room temperature. Another aqueous solution of 2.00 mmol (0.484 g) sodium molybdate [$Na_2MoO_4 \cdot H_2O$, Merck, Germany] in 20 ml DI water was added dropwise to the above solution. After 30 minutes of vigorous stirring, the resulting solution turned a pale yellow colour; the solution was then transferred to a Teflon autoclave for hydrothermal reaction at 180 °C for 24 h. The final product was

collected by centrifugation, followed by simultaneous washing with DI water and ethanol, overnight drying at 70 °C and calcination at 800 °C for 5 h in a muffle furnace. The synthesis was repeated using different concentrations of $Na_3Cit \cdot 2H_2O$ (0.00, 0.50, 0.78, and 1.00 mmol, *i.e.*, 0.00, 0.147, 0.229, and 0.294 g) to examine its effect on the final product, and the resulting samples were labelled as $NCMO_{0.00}$, $NCMO_{0.50}$, $NCMO_{0.78}$ and $NCMO_{1.00}$, respectively. The reaction procedure is presented schematically in Fig. S1 of the ESI.†

## 2.2 Characterization and gas-sensing properties

X-Ray diffraction (XRD) patterns were obtained using a Rigaku Ultima III powder diffractometer equipped with $CuK_\alpha$ radiation ($\lambda = 1.54056$ Å) and utilized to examine the phase purity and other crystallographic information through the Rietveld refinement method using the FullProf program suite. Experimental profiles were fitted with a suitable pseudo-Voigt analytical asymmetric function, while the background was fitted with a fourth-order polynomial function. Field emission scanning electron microscopy (FESEM: Hitachi S – 4800, operated at 5 kV) was used to inspect the morphology of the samples, while a transmission electron microscope (TEM-2100 Plus Electronmicroscope, 200 kV) was used to obtain high-resolution microscopic images and selected area electron diffraction (SAED). Raman spectra obtained using an alpha 300 Witec with a 530 nm laser (power: 3 mW; spot size: 2 μm) and Fourier transform infrared (IR) spectra recorded using an IR Prestige were utilized to examine the short-range structural distortion. X-Ray photoelectron spectra (XPS) were collected using a PHI Versa Probe III Scanning XPS Microprobe with an Al K source. The optical properties of the as-prepared samples were investigated at room temperature using UV-Vis spectroscopy (JASCO V650) and photoluminescence spectroscopy (FP-8300, JASCO, 100 W Xe lamp).

Gas-sensing properties were examined using Taguchi-type sensor module, in which a hollow cylindrical $Al_2O_3$ substrate having Pt electrodes was coated with a thick slurry of the nanostructured NCMO materials through the drop-casting method. The slurry was prepared by mixing the as-prepared samples with isopropyl alcohol as a binder, and the coated substrates were heated at 100 °C for 12 h to remove residual solvents. Ni–Cr wire was inserted through the hole of the substrate as a heating element to provide the required temperature by adjusting the applied voltage across the wire. Gases supplied from cylinders, balanced with air, were used during measurement of the sensing performance with an Agilent 34461A digital multimeter interfaced with data logger software.

## 2.3 Calculation of band structure and investigation of gas-sensing mechanism using *ab initio* density functional theory

It is well-known that the electronic band structure provides theoretical insight into the opto-electronic properties of any material; hence, we computed the spin-polarized band structure, density of states (DOS), partial DOS (pDOS), total DOS (TDOS) and projected DOS (PDOS) using VASP.[21] Here, the

plane-wave pseudo-potential (PAW) was used, while the Perdew–Burke–Ernzerhof (PBE) exchange correlation and ultra-soft potential as basis set were considered.[22] We employed the valence electrons of the respective atoms as follows: Na atom ($1s^2\ 2s^2\ 2p^6\ 3s^1$), Ce atom ($5s^2\ 5p^6\ 4f^1\ 5d^1\ 6s^2$), Mo atom ($4p^6\ 5s^2\ 4d^{10}$), and O atom ($2s^2\ 2p^4$). For this calculation, $5 \times 5 \times 7$ Monkhorst–Pack $k$ points were used, as this allowed an accurate representation of the Brillouin zone and the electronic properties of the material. Prior to calculating the band structure along $\Gamma \rightarrow X \rightarrow H_1 \rightarrow C \rightarrow H \rightarrow Y \rightarrow \Gamma$, the structure was optimized with the lowest single-point ground state energy by fixing the cut-off energy at 520 eV, while the convergence was tested between 220 and 620 eV. A maximum atomic displacement of $\sim 5 \times 10^{-4}$ Å and stress of $\sim 0.02$ GPa were considered for this calculation. Each atom was exposed to a 0.01 eV Hellmann–Feynman force to ensure stable convergence, while the EDIFF and force EDIFG parameters were adjusted to $10^{-6}$ eV and $10^{-3}$ eV, respectively, to ensure high-precision computational convergence.[14]

In order obtain theoretical insight into the influence of the defects on the gas-sensing performance, we calculated the adsorption energies of acetone on the NCMO surface as shown in Table S2 (ESI†). Herein, we have modelled the tetragonal NCMO (112) plane with supercell dimension of 7.573 Å $\times$ 17.823 Å $\times$ 32.422 Å. The $k$-point mesh for this calculation was optimized at $3 \times 3 \times 1$, while the thickness of the slab and the vacuum level were $\sim 3$ nm and 15 Å, respectively. In these calculations, the bottom half of the layers were frozen, whereas the top half of the layers with acetone as the adsorbent were set to relax. The adsorption energy was then calculated using eqn (1):

$$E_{ads} = E_{NCMO+acetone} - E_{NCMO} - E_{acetone} \qquad (1)$$

where $E_{NCMO+acetone}$, $E_{NCMO}$ and $E_{acetone}$ represent the total ground state energies of NCMO in combination with the acetone molecule, bare NCMO and acetone gas, respectively. In order to examine the influence of defects on the gas-sensing activity, we carried out the above calculations by removing one or two oxygen atoms from the (112) plane of NCMO, as shown in Fig. S2 (ESI†).

## 3. Results and discussion

### 3.1 Structural and morphological studies using XRD, FESEM and TEM

The XRD patterns of all the samples (Fig. 1) closely match with that of scheelite-type tetragonal NCMO with the space group $I4_1/a$ ($C_{4h}^6$, ICDD Database No. 04-007-5489). The absence of any peak other than those of NCMO confirms the phase purity of the synthesized nanostructures, while the sharp diffraction
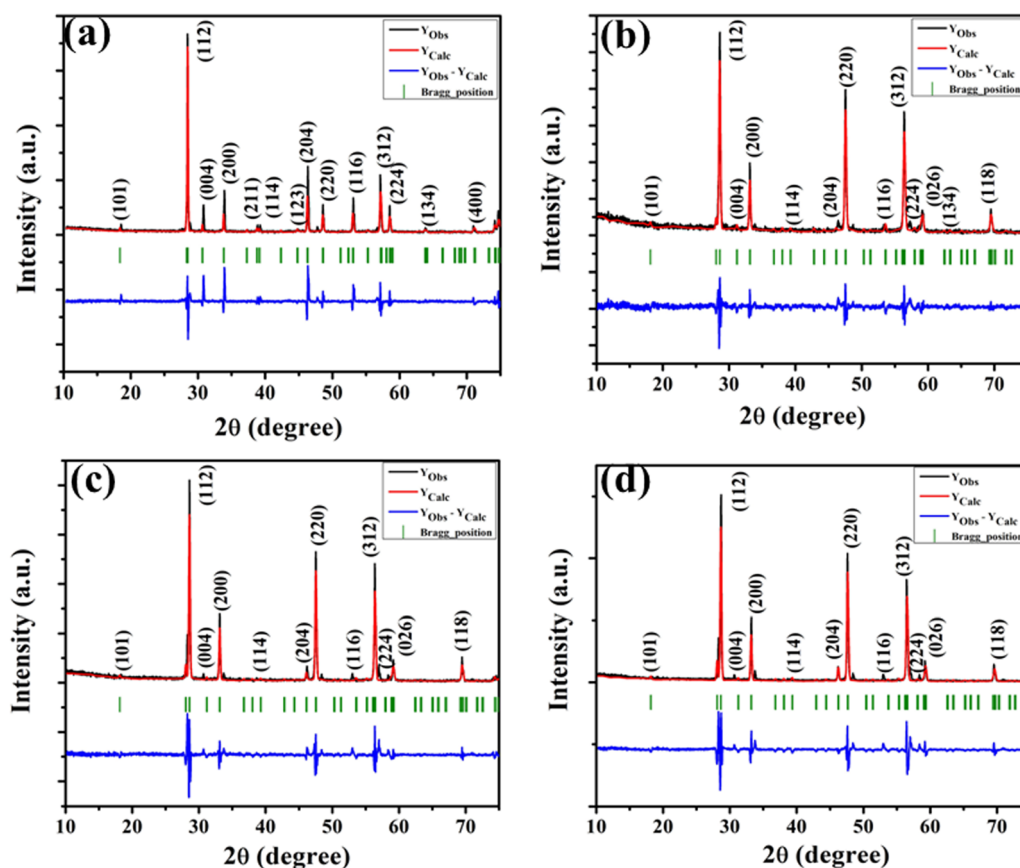


Fig. 1 XRD patterns of the NaCe(MoO$_4$)$_2$ samples (a) NCMO$_{0.00}$, (b) NCMO$_{0.50}$, (c) NCMO$_{0.78}$ and (d) NCMO$_{1.00}$, respectively.

peaks indicate good crystallinity. The unit cell is represented in Fig. S3, and Table S1 in the ESI† summarizes the structural parameters as obtained from Rietveld refinement, which was carried out until satisfactory convergence of $\chi^2$, $R_p$ and $R_{wp}$ were achieved.[23] As shown in Fig. S3 (ESI†), the unit cell of NCMO comprises Na and Ce atoms at the 4b sites and is coordinated to eight O atoms at 16f site *via* two different bond lengths to produce $(Na/Ce)O_8$ polyhedra; in turn, these polyhedrons are connected to $MoO_4$ tetrahedra with Mo at the 4a site. The unit cell volume, $c$ value, $c/a$ ratio, Na/Ce–O bond lengths, and the Na/Ce–O–Mo and O–Mo–O bond angles (but not the Mo–O bond lengths) decrease monotonically from $NCMO_{0.00}$ to $NCMO_{1.00}$, indicating an enhancement in the distortion of the unit cells. The $(Na/Ce)O_8$ polyhedral ($N$) and $MoO_4$ tetrahedral ($K$) distortions were calculated using the expressions $N = \dfrac{\alpha_{1(O-Mo-O)}}{\alpha_{2(O-Mo-O)}}$,[24] where $\alpha_{1(O-Mo-O)}$ and $\alpha_{2(O-Mo-O)}$ denote the two different bond angles, and $K = \dfrac{d_{1(Na,Ce-O)}}{d_{2(Na,Ce-O)}}$, where $d_{1(Na,Ce-O)}$ and $d_{2(Na,Ce-O)}$ represent the two different bond lengths and were found to be $N$ = 1.011, 1.029, 1.043, 1.052 and $K$ = 1.0587, 1.0827, 1.0838, 1.0842 for $NCMO_{0.00}$, $NCMO_{0.50}$, $NCMO_{0.78}$ and $NCMO_{1.00}$, respectively.[25,26] According to previous studies, a decrease in the $c/a$ ratio is associated with the partial substitution of $Na^+$ by $Ce^{3+}$,[27,28] while the perquisite charge neutrality is balanced by O vacancies ($V_O$), causing increases in $K$ and $N$.

It can be noted from the FESEM image that $NCMO_{0.00}$ possesses an irregular shape (Fig. 2(a)), while a gradual transformation from an irregular to a truncated octahedral shape was observed for $NCMO_{0.50}$, $NCMO_{0.78}$ and $NCMO_{1.00}$ (Fig. 2(b)–(d)) suggesting that $Na_3Cit$ has significant role during hydrothermal reaction to tune morphology. Mapping of the samples (Fig. S4, ESI†) clearly reveals even distribution of elements. For a better understanding of the shape of these microstructures, transmission electron microscopy (TEM) was further employed. Fig. 2(e) depicts a typical TEM image of $NCMO_{1.00}$, which corroborates the truncated octahedral shape, while the selected area diffraction pattern (Fig. 2(f)) consists of five diffraction spots corresponding to the (112), (211), (123), (222) and (224) planes of tetragonal NCMO, denoting its crystalline character.

### 3.2 Investigations of local structure using FTIR, Raman and X-ray photoelectron spectroscopies

To understand the influence of $V_O$ on the short-range structural distortions of $(Na/Ce)O_8$ polyhedra and $MoO_4$ tetrahedra, we obtained the FTIR and Raman spectra of our synthesized samples. The various peaks in the absorption band (shown in Fig. S5 of the (ESI†)) between 500 and 1000 $cm^{-1}$ are attributed to the various active internal vibrations of $MoO_4$ tetrahedra. Commonly, $MoO_4$ tetrahedra crystallize in either regular $(Mo^RO_4)$ or distorted form $(Mo^DO_4)$ due to $V_O$, while the vibration ($\Gamma_{Td}$) of the isolated $Mo^RO_4$ is represented by:[29]

$$\Gamma_{Td} = A_1 + E + 2F_2 \qquad (2)$$
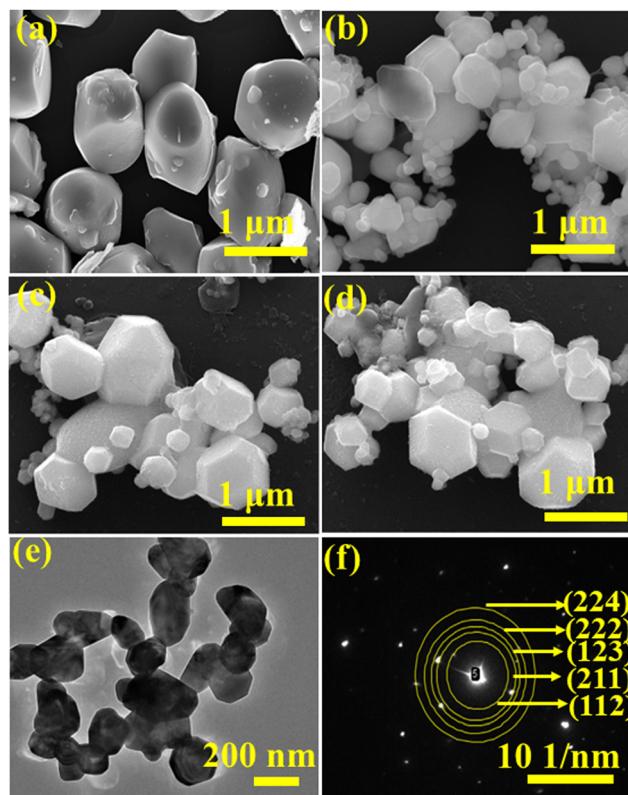


**Fig. 2** FESEM images of NCMO samples (a) $NCMO_{0.00}$, (b) $NCMO_{0.50}$, (c) $NCMO_{0.78}$ and (d) $NCMO_{1.00}$, (e) and (f) TEM image and SAED pattern of $NCMO_{1.00}$.

However, the symmetry of the tetrahedra changes to $S_4$ in NCMO, for which the IR active modes include $\nu_1(A_1)$, $\nu_2(E_1)$, $\nu_3(F_2)$, $\nu_4(F_2)$, one free rotation $\nu_{f.r.}(F_1)$ and one translation $F_2$. In contrast to $Mo^RO_4$, $Mo^DO_4$, which has the $C_{2h}^6$ space group, exhibits four formula units per crystallographic unit cell with $2Mo(C_2)$, $4Mo(C_1)$, $4Ce(C_1)$ and $24O(C_1)$ symmetries of the atoms, indicating splitting of the vibrational modes (*i.e.*, $O \rightarrow Mo(C_1) \rightarrow O$ and $O \rightarrow Mo(C_2) \rightarrow O$) within $Mo^DO_4$ due to lower site symmetry.[30] The two bands at 650–749 and 750–1000 $cm^{-1}$ are ascribed to $\nu_3(F_2)$ and $\nu_4(F_2)$, while the peak at 670 $cm^{-1}$ is assigned to $\nu_2(E_1)$. Careful deconvolution (Fig. S6, ESI†) of the $\nu_3(F_2)$ and $\nu_4(F_2)$ modes yields three peaks (*i.e.*, 693, 705, 722 $cm^{-1}$ and 813, 858, 909 $cm^{-1}$). As per the bond length–stretching frequency correlation described by Hardcastle *et al.*, an increase in the bond length decreases the vibrational frequency.[31] Hence, the vibrational mode with lower energy corresponds to $Mo^DO_4$, while the high-energy peaks are ascribed to $Mo^RO_4$. Therefore, the peaks at 722 and 909 $cm^{-1}$ are attributed to the $\nu_3(F_2)$ and $\nu_4(F_2)$ modes of $Mo^RO_4$, respectively, while the peaks at 693/705 $cm^{-1}$ and 813/858 $cm^{-1}$ correspond to the $\nu_3(F_2)$ and $\nu_4(F_2)$ mode of vibration within $Mo^DO_4$.[30] The $Mo^DO_4/Mo^RO_4$ ratio, which was calculated from the areas under the curve, was found to be 0.8, 1.0, 1.6 and 2.9 for $NCMO_{0.00}$, $NCMO_{0.50}$, $NCMO_{0.78}$ and $NCMO_{1.00}$, respectively, indicating an increase in tetrahedral distortion with increasing $Na_3Cit$ concentration, which corroborates the previous structural studies using XRD.

The Raman spectra, which were obtained up to the range of 1000 cm$^{-1}$ at ambient temperature (Fig. S7, ESI†), consist of a peak at 463 cm$^{-1}$ and three bands at 64–231, 255–425 and 681–966 cm$^{-1}$. In general, Raman spectra of scheelite materials at the $\Gamma$-point is expressed as:

$$\Gamma = 3A_g + 5B_g + 5E_g \qquad (3)$$

where the non-degenerate $A_g$ and $B_g$ modes and the doubly degenerate $E_g$ mode correspond to the various external and internal vibrations of $MoO_4$ and $CeO_8$.[29] The peak at 64–231 cm$^{-1}$ corresponds to the rotation and translation of the $MoO_4$ tetrahedra and $Na^+$ and $Ce^{3+}$, respectively. The sharp peak is attributed to the external vibration of $CeO_8$, which is in good agreement with previous results,[32] while the bands are ascribed to the internal bending of the $MoO_4$ tetrahedra. After thorough examination, the two peaks at 318 and 380 cm$^{-1}$ were assigned to the symmetric $A_g$ bending and antisymmetric $B_g$ bending vibrational modes of $MoO_4$, respectively.[33] While the peak at 463 cm$^{-1}$ is assigned to antisymmetric $A_g$ bending mode of $MoO_4$. The other two Raman peaks at 823 and 889 cm$^{-1}$ are assigned to (O → Mo → O) antisymmetric stretching $B_g$ and (O ← Mo → O) symmetric $A_g$ mode of vibration.[29,34,35] The decrease in Raman intensity with increasing $Na_3Cit$ concentration is believed to be related to the increase of $V_O$ and antisite defects, in agreement with the XRD and FTIR studies.[36,37]

X-Ray photoelectron spectroscopy (XPS), a well-known technique to investigate the chemical state of elements, was adopted here to examine $V_O$-associated changes in the valence states of Na, Ce, Mo and O, as they are highly sensitive to the local electronic environment. The binding energy data of all elements were adjusted with respect to the binding energy ($\sim$284.6 eV) of surface-adsorbed atmospheric C 1s.[14] The survey scans for all the synthesized samples are presented in Fig. S8 of the ESI,† while the high-resolution spectra of Mo, Ce, and O are illustrated in Fig. S9–S11 of the ESI.† Two peaks (i.e., 232.7 and 236.0 eV) of Mo can be readily ascribed to the spin–orbit splitting of the $3d_{5/2}$ and $3d_{3/2}$ orbitals of $Mo^{6+}$, while careful deconvolution (Fig. S9(a)–(d), ESI†) reveals the presence of two peaks for the two orbitals (i.e., 232.5 and 232.9 eV for $3d_{5/2}$ and 235.7 and 236.2 eV for $3d_{3/2}$), which were assigned as $Mo3d_{5/2}(I)$, $Mo3d_{5/2}(II)$ and $Mo3d_{3/2}(I)$, $Mo3d_{3/2}(II)$, respectively. Accordingly, we ascribed $Mo3d_{5/2}(II)$ and $Mo3d_{3/2}(II)$ to $Mo^R O_4$, while $Mo3d_{5/2}(I)$ and $Mo3d_{3/2}(I)$ corresponded to $Mo^D O_4$; their difference can be assigned to the $V_O$-induced changes in electronic repulsion. In brief, electrons are located on O due to its strong electronegativity, which makes the Mo–O bond significantly ionic, while $V_O$ increases the effective charge on Mo. Hence, the electron–electron repulsion on Mo reduces the binding energies of the Mo $3d_{5/2}$ and $3d_{3/2}$ orbitals in $Mo^D O_4$. In this context, the smaller energy difference between $3d_{5/2}$ and $3d_{3/2}$ in $Mo^D O_4$ with respect to $Mo^R O_4$ (i.e., 3.23 and 3.19 eV) again indicates the influence of the local field generated from $V_O$ on spin–orbit splitting. The weighted percentage of $Mo^D O_4$ calculated from the area under the curve was found to be $\sim$26, 32, 35 and 42% for $NCMO_{0.00}$, $NCMO_{0.50}$, $NCMO_{0.78}$ and $NCMO_{1.00}$, respectively, which agrees well with the previous
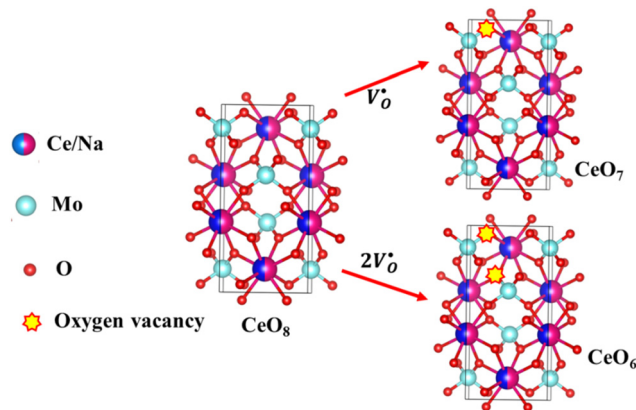


Fig. 3 Schematic diagram of oxygen vacancies of the $CeO_8$ polyhedral unit.

finding of increasing $Mo^D O_4$ content. As illustrated in Fig. S10(a)–(d) (ESI†), the two asymmetric peaks observed at 877–891 and 894–912 eV are attributed to the spin–orbit splitting of the $3d_{5/2}$ and $3d_{3/2}$ orbitals of $Ce^{3+}$. Similar to the Mo orbitals, careful deconvolution of the asymmetric $d_{5/2}$ peak yields three peaks at 882.0, 884.6, and 886.9 eV, which were designated as $Ce3d_{5/2}(I)$, $Ce3d_{5/2}(II)$ and $Ce3d_{5/2}(III)$, indicating the presence of Ce with three different oxidation states. $Ce3d_{5/2}(III)$ was assigned to the Ce of the regular $CeO_8$ polyhedra, while $Ce3d_{5/2}(II)$ and $Ce3d_{5/2}(I)$ correspond to Ce belonging to the $CeO_8$ polyhedra with one or two oxygen vacancies (ca. $V_O$ and $2V_O$) and with the nomenclature $CeO_7$ and $CeO_6$, respectively. In this context, it may be stated that $CeO_7$ and $CeO_6$ represent deformed $CeO_8$ polyhedra with one or two nearby $Mo^D O_4$ and $Mo^D O_4$ subunits (shown schematically in Fig. 3). Due to smaller difference in electronegativity between Ce and O, the Ce–O bond is supposed to be more covalent; therefore, $V_O$ plays the predominant role in terms of this covalence and the binding energy. We observed from the Rietveld analysis that $V_O$ shortens Ce–O bond lengths, which in consequence increases electron–electron repulsion at Ce site; thus, the binding energy of the 3d orbitals is decreased in the distorted polyhedra.[38] The analysis showed that the weighted percentage of $Ce_a$ increases ($\sim$19, 23, 37, 41%), while there is a significant decrease in the weighted percentage of $Ce_b$ ($\sim$48, 46, 37, 26%) from $NCMO_{0.00}$ to $NCMO_{1.00}$. On the other hand, $Ce_c$ remains almost unchanged for all samples ($\sim$30%). Therefore, the analysis indicates greater generation of $2V_O$ at the cost of $V_O$; hence, the tendency for $V_O$ cluster formation increases. The XPS of O 1s displays asymmetry, indicating the presence of two different O species. A careful analysis reveals two O 1s peaks (Fig. S11, ESI†) at 530.6 and 532.4 eV, corresponding to lattice O and the O atom of the $Mo^D O_4$ tetrahedra.[39] The increasing ratio of the area under the fitted curves illustrates the monotonic increase in $Mo^D O_4$ tetrahedra from $NCMO_{0.00}$ to $NCMO_{1.00}$.

### 3.3 Optical properties of the as-prepared NCMO samples using UV-Vis and photoluminescence spectroscopy

The optical band gap ($E_g$) was calculated to be $\sim$3.07, 3.05, 3.02 and 2.99 eV for $NCMO_{0.00}$, $NCMO_{0.50}$, $NCMO_{0.78}$ and $NCMO_{1.00}$

based on the UV-Vis absorption spectra (shown in Fig. S12, ESI†). This variation can be understood as follows: our band structure calculations (discussed later) reveal that the valence band (VB) is made up of O 2p–Mo 4d hybridization, while the conduction band (CB) comprises Mo 4d, Ce 4f and a minute contribution from O 2p orbitals. The decrease of Mo–O bond length in the presence of $V_O$ and $2V_O$ reduces the O 2p–Mo 4d overlap, which causes a blue-shift of the VB, and subsequently, $E_g$ is reduced. All the samples exhibit a broad peak at 380 nm in their photoluminescence excitation (PLE) spectra, which were obtained using an emission wavelength $\lambda_{em}$ of 531 nm (Fig. S13, ESI†), while the emission spectra recorded in the visible region using an excitation wavelength of $\lambda_{ex} = 380$ nm are depicted in Fig. 4(a)–(d). The PLE peak was assigned to

O 2p–Mo 4d charge transfer absorption within $MoO_4$ tetrahedra.[40,41] The emission spectra have four distinct peaks in the blue (i.e. blue I, blue II, blue III) and green regions, with an intense blue I peak being observed at 440 nm ($22\,727$ cm$^{-1}$), while relatively weaker blue II, blue III peaks and a prominent green peak are observed at 462 nm ($21\,645$ cm$^{-1}$), 488 nm ($20\,492$ cm$^{-1}$) and 531 nm ($18\,832$ cm$^{-1}$), respectively. The Stokes shift of the excitation and emission spectra were noted to be $\sim 3588$ cm$^{-1}$, suggesting the absence of reabsorption and interference among the various emissions.[42] Although understanding the emission spectra of lanthanides is difficult for several reasons, including symmetry, the crystal field surrounding the host crystal, anion polarizability, and covalence of the host crystal, the present emissions are believed to be 5d–4f
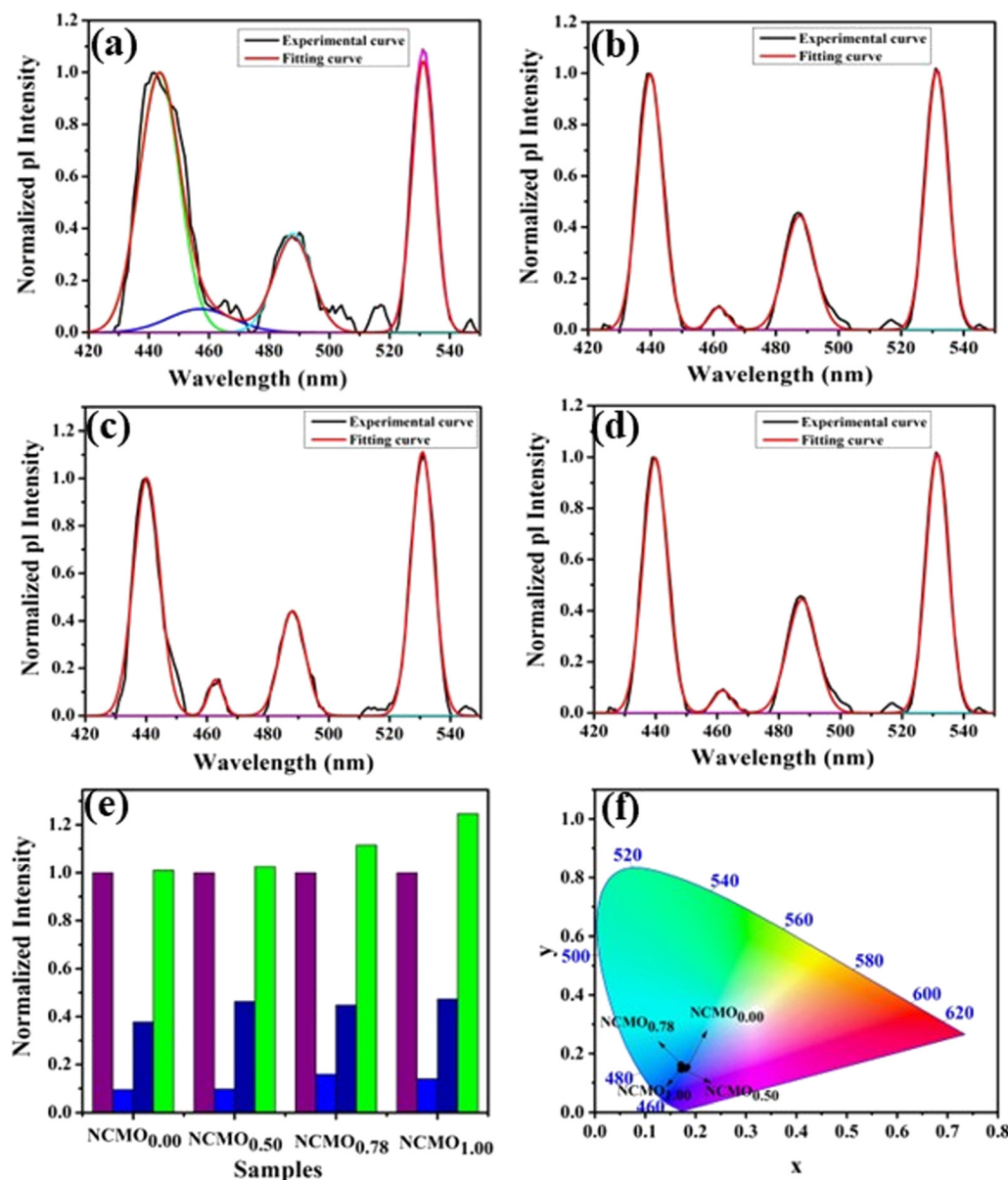


Fig. 4 Photoluminescence spectra of (a) NCMO$_{0.00}$, (b) NCMO$_{0.50}$, (c) NCMO$_{0.78}$ and (d) NCMO$_{1.00}$. (e) Normalized PL intensity ratio of emission wavelengths. (f) CIE chromaticity diagram of the NCMO phosphors.

transitions within $Ce^{3+}$[43] and can be validated as follows. The emission wavelength ($\lambda$ in nm) for intra-5d–4f transitions can be calculated using eqn (4):[44,45]

$$\frac{1}{\lambda} = \frac{Q^*}{hc}\left[1 - \left(\frac{V}{4}\right)^{\frac{1}{V}} 10^{\frac{-(nrE_a)}{80}}\right] \quad (4)$$

where, $Q^*$, $V$, '$n$', $E_a$ and '$r$' represent the energy of the 5d band edge of a free $Ce^{3+}$ ion (= 50 000 $cm^{-1}$), the valence of the $Ce^{3+}$, the number of anions in the immediate shell around the $Ce^{3+}$, the electron affinity of the atoms forming the anions ($\sim 2.16$ eV) and the difference between the average bond length and radius of $Ce^{3+}$ within the $CeO_8$ polyhedra (1.03 Å). Very careful calculation yields $\lambda \sim 449$ nm, which corresponds to blue I emission. Previous studies indicate that $V_O$ and $2V_O$ can significantly modify the 5d–4f transitions of lanthanide atoms, resulting in different emissions. As an example, Sokolenko et al.[46] assigned green–red emission to $WO_3 \cdot V_O^{\bullet\bullet}$ oxygen-deficient complexes, while Korzhik et al. ascribed green emission to $WO_3$ centres.[47] Considering $CeO_7$ and $CeO_6$ to be $V_O$- and $2V_O$-containing distorted $CeO_8$ polyhedra, we have calculated $\lambda$ values of 487 and 537 nm for intra-$Ce^{3+}$ 5d–4f transitions using eqn (4), which are in good agreement with the blue III and green emissions (schematically represented in Fig. S14, ESI†).

The shift of the centroids of the d-orbitals (in eV) of $Ce^{3+}$, $\varepsilon_c(1,3+,Ce^{3+})$ in $CeO_7$ and $CeO_6$ are believed to tune the 5d–4f transition, giving various emissions (see discussion in the ESI†). Careful monitoring of the green emission reveals the presence of a phonon side band (PSB) at 516 nm with a phonon energy of 930 $cm^{-1}$, which exactly matches the energy of the $\nu_4(F_2)$ phonon mode, indicating that $MoO_4 \rightarrow CeO_6$ charge transfer is mediated by the $\nu_4(F_2)$ phonon mode. In this context, the Huang–Rhys ($S$) factor, an indicator of electron–phonon coupling, was calculated using eqn (5) and (6):[48,49]

$$S = \frac{I_{PSB}}{I_{ZP}} \quad (5)$$

$$\frac{I_{1P}}{I_{ZP}} = \frac{W_1(S, \langle m \rangle)}{W_0(S, \langle m \rangle)} = \begin{cases} S\langle 1+m \rangle, & p \geq 0 \\ S\langle m \rangle, & p < 0 \end{cases} \quad (6)$$

where, $I_{PSB}$, $I_{ZP}$ and $I_{1P}$ are the integrated intensities of the PSB, zero-phonon line and one-phonon line. As this emission includes a single phonon ($p \geq 0$ in eqn (6)), and considering the $^5D_0$–$^2F_{5/2}$ transition to be purely dipolar, we may write $I_{PSB} = I_{1P}$. In addition, $\langle 1+m \rangle$ can also be considered to be 1 due to the higher phonon energy at room temperature. The decrease in the $S$-factor (0.098, 0.077, 0.032 and 0.039 for the four respective samples) is ascribed to increasing distortion in the lattice structure due to $V_O$ and $2V_O$.

The Commission International De l'Eclairage (CIE) coordinates (Fig. 4(f)), which were calculated to be (0.180, 0.149), (0.180, 0.147), (0.170, 158) and (0.172, 0.148) for the $NCMO_{0.00}$, $NCMO_{0.50}$, $NCMO_{0.78}$ and $NCMO_{1.00}$ samples, are well spread throughout the blue region of the visible spectrum, indicating the color purity (CP) of the NCMO samples.[50] We also validated

the CP using eqn (7):[51,52]

$$CP = \frac{\sqrt{(x - x_i)^2 + (y - y_i)^2}}{\sqrt{(x_d - x_i)^2 + (y_d - y_i)^2}} \times 100\% \quad (7)$$

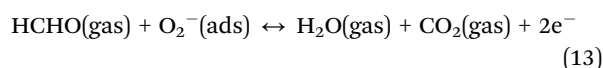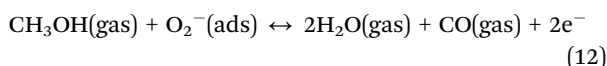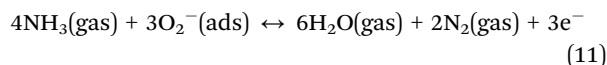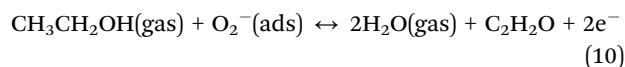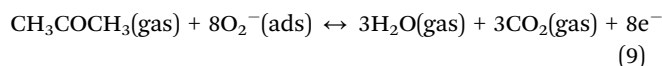where $(x, y)$ denotes the color coordinates of the phosphor; $(x_i, y_i)$ is the 1931 CIE Standard Source's illuminant point, with color coordinates of (0.3101, 0.3162); and $(x_d, y_d)$ is the color coordinates of the dominant wavelength. Outstanding CP values of $\sim 90$–94% were observed for the samples, indicating that NCMO could be a good candidate for blue-light-emitting applications. The correlated colour temperature (CCT) was calculated using McCamy's relation:[53]

$$CCT = 449n^3 + 3525n^2 + 6823.3n + 5520.3 \quad (8)$$

where $n = \frac{(x - 0.3320)}{(0.1858 - y)}$ and $(x, y)$ represent the chromaticity co-ordinates. The CCT values were $\sim 7819$ K, 7630 K, 7715 K and 7854 K for the samples $NCMO_{0.00}$, $NCMO_{0.50}$, $NCMO_{0.78}$ and $NCMO_{1.00}$, respectively. The high CCT indicates that NCMO can be used for cold blue lighting.

### 3.4 Investigations of gas-sensing properties of NCMO nanostructures

The gas-sensing abilities of metal oxide nanostructures involve a solid–gas interfacial reaction mechanism in which the adsorption/desorption of the targeted gas molecules on the surface of the nanostructure leads to significant changes in resistance. A careful literature survey indicates that the following redox reactions between the nanostructure and acetone ($CH_3COCH_3$), ethanol ($C_2H_5OH$), ammonia ($NH_3$), methanol ($CH_3OH$), formaldehyde (HCHO) take place in the presence of $O_2^-$(ads).

$$CH_3COCH_3(gas) + 8O_2^-(ads) \leftrightarrow 3H_2O(gas) + 3CO_2(gas) + 8e^- \quad (9)$$

$$CH_3CH_2OH(gas) + O_2^-(ads) \leftrightarrow 2H_2O(gas) + C_2H_2O + 2e^- \quad (10)$$

$$4NH_3(gas) + 3O_2^-(ads) \leftrightarrow 6H_2O(gas) + 2N_2(gas) + 3e^- \quad (11)$$

$$CH_3OH(gas) + O_2^-(ads) \leftrightarrow 2H_2O(gas) + CO(gas) + 2e^- \quad (12)$$

$$HCHO(gas) + O_2^-(ads) \leftrightarrow H_2O(gas) + CO_2(gas) + 2e^- \quad (13)$$

Our previous investigations indicate that $V_O$ and $2V_O$ defects are often ionized (e.g., $CeO_7 \cdot V_O^{\bullet}$, $CeO_6 \cdot 2V_O^{\bullet}$) and act as electron donors ($[CeO_8]'$ and $[CeO_8]''$), which can be understood from Kröger–Vink notation:

$$[CeO_8]^x + [CeO_7 \cdot V_O^x] \rightarrow [CeO_8]' + [CeO_7 \cdot V_O^{\bullet}] \quad (14)$$

$$[CeO_8]^x + [CeO_6 \cdot 2V_O^x] \rightarrow [CeO_8]'' + [CeO_6 \cdot 2V_O^{\bullet}] \quad (15)$$

These $[CeO_8]'$ and $[CeO_8]''$ facilitate electron transfer from the host materials to the chemisorbed oxygen molecule to generate $O_2^-$(ads), as described by the reaction: $O_2(gas) + e^- \leftrightarrow O_2^-(ads)$.[54–57]
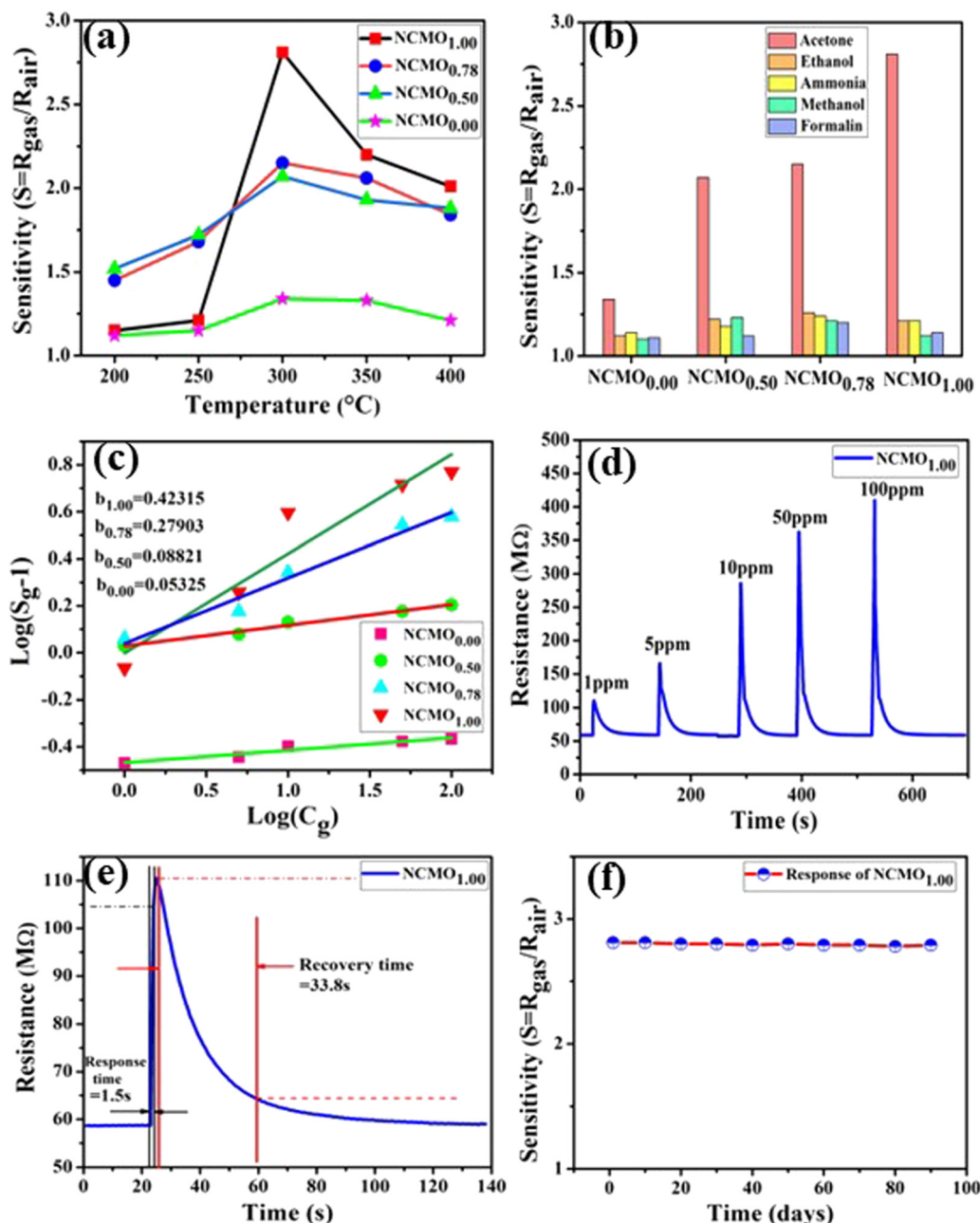
Fig. 5 (a) Temperature calibration curves of $NCMO_{0.00}$, $NCMO_{0.50}$, $NCMO_{0.78}$ and $NCMO_{1.00}$, respectively. (b) Selectivity of $NCMO_{0.00}$, $NCMO_{0.50}$, $NCMO_{0.78}$ and $NCMO_{1.00}$ sensors measured at an operating temperature of 300 °C. (c) Linear fitting of the logarithm of sensitivity and logarithm of acetone concentration data of all samples. (d) Dynamic acetone response curves of the $NCMO_{1.00}$ sensor to acetone concentrations from 1–100 ppm at 300 °C. (e) Response and recovery time of the $NCMO_{1.00}$-based sensor for 1 ppm acetone at 300 °C. (f) Long-term stability of the $NCMO_{1.00}$-based sensor in sensing 1 ppm acetone measured over 90 days.

In order to validate the gas-sensing ability of our synthesized NCMO nanostructures as a proof of concept, we carried out a series of sensing measurements using $NCMO_{0.00}$, $NCMO_{0.50}$, $NCMO_{0.78}$ and $NCMO_{1.00}$ as a resistive sensor probe against $NH_3$, $CH_3COCH_3$, $C_2H_5OH$, $CH_3OH$ and $HCHO$ at different operating temperatures (200–450 °C) at intervals of 50 °C. An optimum operating temperature of $\sim$300 °C was observed for all the samples (shown in Fig. 5(a)), and they are highly selective toward $CH_3COCH_3$ (Fig. 5(b), 5.0 ppm concentration) in comparison with

$C_2H_5OH$, $NH_3$, $CH_3OH$, and $HCHO$ $\left( \dfrac{R_{gas}}{R_{air}} < 1.2 \right)$. The sensitivity monotonically increases from $NCMO_{0.00}$ to $NCMO_{1.00}$, with the highest sensitivity being observed for $NCMO_{1.00}$. To understand the role of $V_O$, $2V_O$ in $CH_3COCH_3$ adsorption/desorption, we fitted the response data using the Freundlich adsorption isotherm as given in eqn (16) and (17).

$$S_g = 1 + aC_g^{\ b} \tag{16}$$

*i.e.*,

$$\log(S_g - 1) = a + b\log(C_g) \qquad (17)$$

where $S_g$ and $C_g$ represent sensitivity and concentration respectively, while '$a$' and '$b$' are constants that depend on the electrical charge of the species and stoichiometry of the reactions on the surface of the sensing probe. In the literature, '$b$' is noted to be dependent on the adsorbed O species, with $b \leq 0.5$ for $O^{2-}$ adsorption and $\approx 1.0$ for $O^-$ adsorption.[58] From slope of the linear regressions (Fig. 5(c)) curves obtained using eqn (17), we calculated $b$ values of $\sim 0.423$, $0.279$, $0.088$, $0.053$ for $NCMO_{1.00}$, $NCMO_{0.78}$, $NCMO_{0.50}$ and $NCMO_{0.00}$, respectively, suggesting that $2V_O$ acts as a more-active site for $O^{2-}$ generation, facilitating $CH_3COCH_3$ adsorption. The dynamic sensing responses of $NCMO_{1.00}$ (Fig. 5(d)) measured at 300 °C demonstrate sensitivity values of $\sim 1.86$, $2.81$, $4.95$, $6.21$ and $6.89$ in the presence of $1.0$, $5.0$, $10.0$, $50.0$ and $100.0$ ppm of $CH_3COCH_3$, while the response and recovery (at 5.0 ppm of $CH_3COCH_3$, see Fig. S15(b) of the ESI†) remain the same for six consecutive cycles (error $\leq 2\%$), indicating the excellent reproducibility and reliability of $NCMO_{1.00}$ as a sensor probe in comparison with the other samples (Fig. S15(c–e), ESI†). In addition, the very low response and recovery time of $\sim 1.5$ s/33.8 s (Fig. 5(e), measured at 10.0 ppm) indicate the fast response of $NCMO_{1.00}$, while its long-term stability was checked and verified over 90 days at intervals of 10 days (Fig. 5(f)).

### 3.5 Density functional theory (DFT) calculations of NCMO

In order to validate the $V_O$- and $2V_O$-associated optical emissions and sensing activity, we calculated the electronic band structure, total density of states (TDOS), and angular momentum projected partial density of states (PDOS) using *ab initio* density functional theory (DFT), which provides valuable insights to explain the luminescence and gas sensing behaviour. For this, we calculated band structure along several high symmetry $k$-points within the Brillouin zone. In this calculation, we removed one or two O atoms from the NCMO unit cell to mimic $CeO_7$ ($V_O$) and $CeO_6$ ($2V_O$). Prior to calculating the electronic band structure, we optimized the unit cell of pure NCMO and obtained lattice parameters $a = b = 5.355$ and

$c = 11.611$ Å and Na/Ce–O and Mo–O lengths of $\sim 2.453$ and $1.806$ Å, respectively. These were in good agreement with the experimental results, proving the accuracy of our calculations, specifically, the choice of exchange correlation and pseudopotential. The top of the valence band maxima (VBM) was set to zero as a reference for other calculations. As shown in Fig. 6(a), NCMO appears to be an indirect bandgap material ($E_g \sim 3.23$ eV) with a spin-unpolarized VBM and spin-polarized conduction band minima (CBM) at $\Gamma$- and $X$-points, respectively. The curvature of the VBM is observed to be low, indicating a comparatively high effective hole mass, while the CBM has a high curvature suggesting a low effective electron mass. The TDOS (shown in Fig. 6(b)) and PDOS contributions of O, Mo, Ce and Na (shown in Fig. S16(c)–(f), ESI†) demonstrate that the upper part of the VB is primarily composed of the O $2p_x$, $2p_y$, and $2p_z$ orbitals with very small contributions from Mo $2p_x$, $2p_y$, and $2p_z$, giving a low curvature. The lower part of the VB originates from predominant hybridization between Mo $4d_{xy}$, $4d_{xz}$, $4d_{z^2}$ and O $2p_x$, $2p_y$, and $2p_z$ orbitals, whereas $4d_{x^2}$ and $4d_{yz}$ make insignificant contributions. We noted almost no contribution to the VB from the Ce $4f$ and Na $3s$ orbitals. The CBM comprises spin-polarized (*i.e.*, up-spin) Ce $4f_{z^3}$, $4f_{xz^2}$ and $4f_{y^3x^2}$ orbitals, among which the most predominant contribution comes from $4f_{xz^2}$, hybridized with O $2p_x$, $2p_y$, and $2p_z$ orbitals, giving a higher curvature in comparison with the VBM, while the upper portion of the CB is made up of Mo–$4d_{z^2}$ and $4d_{x^2}$. Thus, it may be stated that the $MoO_4$ tetrahedra mostly construct the VB, while the CB is predominantly contributed by the $CeO_8$ polyhedra, and the band-to-band transition includes a Mo $\leftrightarrow$ Ce charge transfer process.

The band structures, TDOS and PDOS of the $V_O^{\bullet}$- and $2V_O^{\bullet}$-containing NCMO samples, designated as $NCMO - V_O^{\bullet}$ and $NCMO - 2V_O^{\bullet}$, are represented in Fig. S17 and S18 (ESI†), respectively. Notably, both the VBM and CBM (shown in Fig. S17(a), ESI†) of $NCMO - V_O^{\bullet}$ remain unchanged, while in case of $NCMO - 2V_O^{\bullet}$, the CBM band has shifted into the $\Gamma$-point (shown in Fig. S17(a), ESI†), indicating the transformation from an indirect to a direct $E_g$ nature for NCMO. We observed an $E_g$ of 3.01 and 2.95 eV for $NCMO - V_O^{\bullet}$ and $NCMO - 2V_O^{\bullet}$, suggesting a decrease in $E_g$ due to $V_O^{\bullet}$ and $2V_O^{\bullet}$. Thus, the
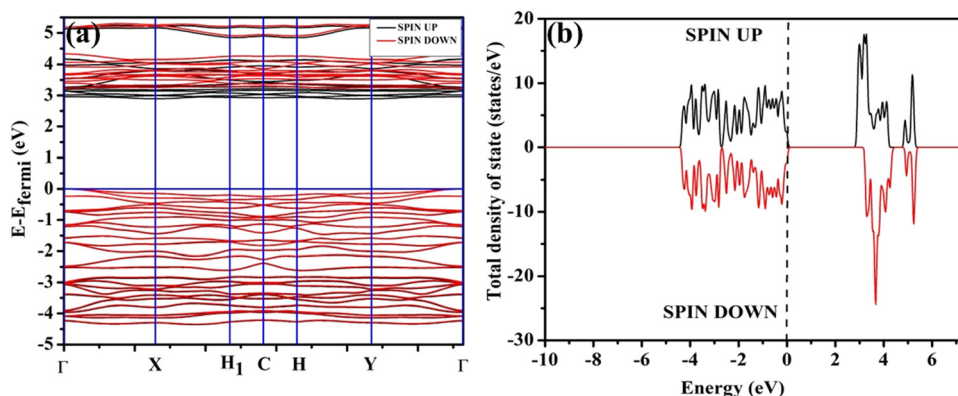
Fig. 6 (a) Band structure and (b) spin-polarised TDOS of NCMO.

monotonic decrease in the experimentally measured $E_g$ from $NCMO_{0.00}$ to $NCMO_{1.00}$ is believed to be due to increasing $V_O$ and $2V_O$, corroborating previous studies. The reduction of $E_g$ can be understood as follows: TDOS (Fig. S17(b) and S18(b), ESI†) and PDOS (Fig. S17(c)–(f) and S18(c)–(f), ESI†) calculations show that the VB width decreases in $NCMO - 2V_O^\bullet$ due to the greater localization of the O 2p orbitals, while the curvature increases in $NCMO - V_O^\bullet$ and $NCMO - 2V_O^\bullet$, which is attributed to the enhanced overlap between the Ce $4f_{zx^2}$, $4f_{xz^2}$, $4f_{yz}$, and $4f_{xyz}$ and O $2p_x$, $2p_y$, and $2p_z$ orbitals due to the decrease in the Ce–O bond length in the $CeO_8$ polyhedra, indicating higher carrier mobility. Further analysis of the TDOS and PDOS reveals that the contributions from Ce $5d_{xy}$ and $5d_{xz}$ to the CB increase in $NCMO - V_O^\bullet$ and $NCMO - 2V_O^\bullet$. The defect state at 2.44 eV above the valence band in $NCMO - V_O^\bullet$ was assigned to Ce $5d_{z^2}$, whilst these defects are found at 2.26 and 2.40 eV above in $NCMO - 2V_O^\bullet$ due to Ce $5d_{z^2}$ and Ce $5d_{x^2}$, respectively. Therefore, it can be stated that the blue III emission originates from Ce $5d_{z^2} \rightarrow$ 4f transitions in the $CeO_7$ polyhedra, while the blue II and green emissions are attributed to Ce $5d_{z^2} \rightarrow$ 4f and Ce $5d_{x^2} \rightarrow$ 4f transitions in the $CeO_6$ polyhedra, respectively, as schematically presented in Fig. 7.

From the calculation of the adsorption energies on the (112) plane with the lowest energy for the NCMO, $NCMO - V_O^\bullet$ and $NCMO - 2V_O^\bullet$ systems using eqn (1), we found the energies listed in Table S2 (ESI†). The $E_{ads}$ (eV) values represent the adsorption energies of the pristine NCMO, $NCMO - V_O^\bullet$, $NCMO - 2V_O^\bullet$ systems, and it was found that $E_{ads} < 0$, indicating that the adsorption processes involved in these systems are thermodynamically stable and exothermic, meaning that they release energy during the adsorption process. Additionally, the increasingly negative values of $NCMO - V_O^\bullet$ and $NCMO - 2V_O^\bullet$ suggest the presence of active sites (oxygen vacancies) on the NCMO surface, which create localized electron-rich sites enabling strong interactions to occur between the $CH_3COCH_3$ and NCMO surfaces.[59] Hence, the highest sensitivity of $NCMO_{1.00}$ (Fig. 5) can purely be assigned to the presence of

the highest $2V_O$ content, which is in good agreement with the experimental results and theoretical calculations.

## 4. Conclusion

In summary, this study reports the synthesis and characterization of oxygen-deficient NCMO-truncated octahedral nanostructures, which exhibit intense blue I and green emissions and comparatively low-intensity blue II and blue III emissions. Excitation involves $MoO_4$ tetrahedra, while emissions are attributed to the 5d $\rightarrow$ 4f transitions of Ce in different $CeO_8$ polyhedral configurations. This study also identified the acetone-sensing ability of NCMO, which has been attributed to $CeO_6$. The valence and conduction bands of NCMO comprise O 2p and O 2p and Ce 5d orbitals, respectively; hence, they are highly sensitive to oxygen vacancies and have a potential role in luminescence and gas sensing. Our study suggests that NCMO may be a promising material for blue-light-emitting and acetone-sensing applications.

## Conflicts of interest

There are no conflicts to declare.

## Acknowledgements

## References

1 B. Glorieux, V. Jubera, A. Apheceixborde and A. Garcia, *Sol. State. Sci.*, 2011, **13**, 460–467.
2 H. Yang, F. Peng, Q. Zhang, W. Liu, D. Sun, Y. Zhao and X. Wei, *Opt. Mater.*, 2013, **35**, 2338–2342.
3 J. R. de Moraes, S. L. Baldochi, L. D. R. L. Soares, V. L. Mazzocchi, C. B. R. Parente and L. C. Courrol, *Mater. Res. Bull.*, 2012, **47**, 744–749.
4 Z. Xu, S. Li, Q. Meng, X. Wang, Q. Zhu and J. G. Li, *J. Alloys Compd.*, 2020, **830**, 154676.
5 J. Kim, *Inorg. Chem.*, 2017, **56**, 8078–8086.
6 F. Cheng, Z. Xia, M. S. Molokeev and X. Jing, *Dalton Trans.*, 2015, **44**, 18078–18089.
7 J. Song, Y. Du, L. Xu, H. Wei, D. He and H. Jiao, *J. Am. Ceram. Soc.*, 2014, **97**, 1442–1449.
8 A. Sarapulova, D. Mikhailova, A. Senyshyn and H. Ehrenberg, *J. Solid State Chem.*, 2009, **182**, 3262–3268.
9 L. S. Cavalcante, J. C. Sczancoski, R. L. Tranquilin, M. R. Joya, P. S. Pizani, J. A. Varela and E. Longo, *J. Phys. Chem. Solids*, 2008, **69**, 2674–2680.
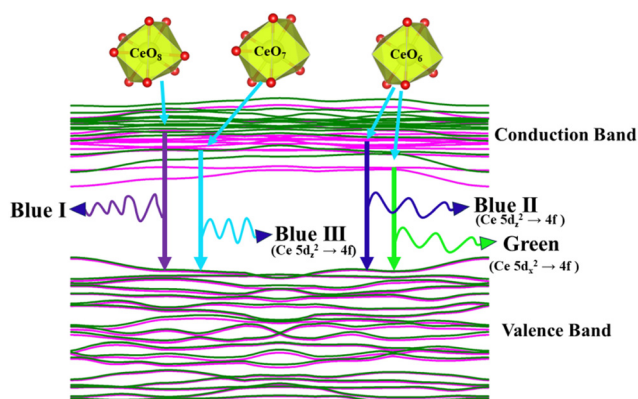
**Fig. 7** Schematic picture of luminescent transitions within different $CeO_8$ polyhedra involving different orbitals.

10 X. Liu, W. Hou, X. Yang and J. Liang, *CrystEngComm*, 2014, **16**, 1268–1276.

11 S. Huang, D. Wang, C. Li, L. Wang, X. Zhang, Y. Wan and P. Yang, *CrystEngComm*, 2012, **14**, 2235–2244.

12 Y. Tian, B. Chen, R. Hua, N. Yu, B. Liu, J. Sun, L. Cheng, H. Zhong, X. Li, J. Zhang and B. Tian, *CrystEngComm*, 2012, **14**, 1760–1769.

13 Z. Wang, Y. Li, Q. Jiang, H. Zeng, Z. Ci and L. Sun, *J. Mater. Chem. C*, 2014, **2**, 4495–4501.

14 N. Haldar, T. Mondal, T. Das, D. Sarkar, M. Pal and C. K. Ghosh, *CrystEngComm*, 2023, **25**, 3514–3527.

15 N. Haldar, T. Mondal, A. Dutta, D. Sarkar, U. K. Ghorai and C. K. Ghosh, *Appl. Phys. A: Mater. Sci. Process.*, 2023, **129**, 708.

16 S. Das, U. K. Ghorai, R. Dey, C. K. Ghosh and M. Pal, *New J. Chem.*, 2022, **46**, 17585–17595.

17 S. Das, U. K. Ghorai, R. Dey, C. K. Ghosh and M. Pal, *Phys. Chem. Chem. Phys.*, 2017, **19**, 22995–23006.

18 B. Ding, H. Qian, C. Han, J. Zhang, S. E. Lindquist, B. Wei and Z. Tang, *J. Phys. Chem. C*, 2014, **118**, 25633–25642.

19 R. Fernández-Climent, S. Giménez and M. García-Tecedor, *Sustainable Energy Fuels*, 2020, **4**, 5916–5926.

20 Z. Lin, M. Xu, Y. Hong, X. Wang and P. Fu, *Mater. Lett.*, 2016, **168**, 72–75.

21 G. Kresse and J. Furthmüller, *Phys. Rev. B: Condens. Matter Mater. Phys.*, 1996, **54**, 11169–11186.

22 G. Kresse and D. Joubert, *Phys. Rev. B: Condens. Matter Mater. Phys.*, 1999, **59**, 1758–1775.

23 W. R. Liu, C. W. Yeh, C. H. Huang, C. C. Lin, Y. C. Chiu, Y. T. Yeh and R. S. Liu, *J. Mater. Chem.*, 2011, **21**, 3740–3744.

24 L. S. Cavalcante, F. M. C. Batista, M. A. P. Almeida, A. C. Rabelo, I. C. Nogueira, N. C. Batista, J. A. Varela, M. R. M. C. Santos, E. Longo and E. M. S. Li, *RSC Adv.*, 2012, **2**, 6438–6454.

25 G. M. Kuzmicheva, A. V. Eremin, V. B. Rybakov, K. A. Subbotin and E. V. Zharikov, *Russ. J. Inorg. Chem.*, 2009, **54**, 854–863.

26 R. L. Andrews, A. M. Heyns and P. M. Woodward, *Dalton Trans.*, 2015, **44**, 10700–10707.

27 L. Li, Y. Su and G. Li, *Appl. Phys. Lett.*, 2007, **90**, 054105.

28 G. M. Kuz'Micheva, I. A. Kaurova, V. B. Rybakov, P. A. Eistrikh-Geller, E. V. Zharikov, D. A. Lis and K. A. Subbotin, *CrystEngComm*, 2016, **18**, 2921–2928.

29 J. V. B. Moura, G. S. Pinheiro, J. V. Silveira, P. T. C. Freire, B. C. Viana and C. Luz-Lima, *J. Phys. Chem. Solids*, 2017, **111**, 258–265.

30 Z. Xu, P. Du, Q. Zhu, X. Li, X. Sun and J. G. Li, *Dalton Trans.*, 2021, **50**, 17703–17715.

31 J. A. Horsley, I. E. Wachs, J. M. Brown, G. H. Via and F. D. Hardcastle, *J. Phys. Chem.*, 1987, **91**, 4014–4020.

32 B. P. Singh and R. A. Singh, *New J. Chem.*, 2015, **39**, 4494–4507.

33 F. F. Wu, D. Zhou, C. Du, S. K. Sun, L. X. Pang, B. B. Jin, Z. M. Qi, J. Varghese, Q. Li and X. Q. Zhang, *J. Mater. Chem. C*, 2021, **9**, 9962–9971.

34 Z. Zhao, Z. Sui, X. Wei, J. Zuo, X. Zhang, R. Dai, Z. Zhang and Z. Ding, *CrystEngComm*, 2015, **17**, 7905–7914.

35 J. Victor-Barbosa-Moura, A. Amison-Gomes-de Souza, P. de Tarso-Cavalcante-Freire, C. da Luz-Lima and T. Mielle-Brito-Ferreira-Oliveira, *Int. J. Appl. Ceram. Technol.*, 2021, **18**, 615–621.

36 Y. Xiong, B. Wang, H. Zhuang, X. Jiang, G. Ma, Y. Yi, W. Hu and Y. Zhou, *RSC Adv.*, 2014, **4**, 36738–36741.

37 N. Dirany, E. McRae and M. Arab, *CrystEngComm*, 2017, **19**, 5008–5021.

38 S. Mandal, C. K. Ghosh, D. Sarkar, U. N. Maiti and K. K. Chattopadhyay, *Solid State Sci.*, 2010, **12**, 1803–1808.

39 T. Thomas, N. Jayababu, J. Shruthi, A. Mathew, A. Cerdán-Pasarán, J. A. Hernández-Magallanes, K. C. Sanal and R. Reshmi, *Thin Solid Films*, 2021, **722**, 138575.

40 A. I. Becerro, M. Allix, M. Laguna, D. González-Mancebo, C. Genevois, A. Caballero, G. Lozano, N. O. Núñez and M. Ocaña, *J. Mater. Chem. C*, 2018, **6**, 12830–12840.

41 L. Xu, G. Liu, H. Xiang, R. Wang, Q. Shan, S. Yuan, B. Cai, Z. Li, W. Li, S. Zhang and H. Zeng, *Appl. Phys. Rev.*, 2022, **9**, 021308.

42 R. Xiao, N. Guo, X. Lv, Q. Ma, B. Shao and R. Ouyang, *Dalton Trans.*, 2022, **51**, 15484–15495.

43 G. Li, Y. Tian, Y. Zhao and J. Lin, *Chem. Soc. Rev.*, 2015, **44**, 8688–8713.

44 Y. Zhu, Y. Liang, M. Zhang, M. Tong, G. Li and S. Wang, *RSC Adv.*, 2015, **5**, 98350–98360.

45 L. G. Van Uitert, *J. Lumin.*, 1984, **29**, 1–9.

46 E. V. Sokolenko, V. M. Zhukovskii, E. S. Buyanova and Y. A. Krasnobaev, *Inorg. Mater.*, 1998, **34**, 499–502.

47 M. V. Korzhik, V. B. Pavlenko, T. N. Timoschenko, V. A. Katchanov, A. V. Singovskii, A. N. Annenkov, V. A. Ligun, I. M. Solskii and J. P. Peigneux, *Phys. Status Solidi A*, 1996, **154**, 779–788.

48 A. Lecointre, A. Bessière, A. J. J. Bos, P. Dorenbos, B. Viana and S. Jacquart, *J. Phys. Chem. C*, 2011, **115**, 4217–4227.

49 J. Raha, N. Haldar and C. K. Ghosh, *Appl. Phys. A: Mater. Sci. Process.*, 2021, **127**, 1–8.

50 S. Das, C. K. Ghosh, R. Dey and M. Pal, *RSC Adv.*, 2016, **6**, 236–244.

51 Y. Shi, Y. Wen, M. Que, G. Zhu and Y. Wang, *Dalton Trans.*, 2014, **43**, 2418–2423.

52 Q. Wang, G. Zhu, Y. Li and Y. Wang, *Opt. Mater.*, 2015, **42**, 385–389.

53 M. Rai, G. Kaur, S. K. Singh and S. B. Rai, *Dalton Trans.*, 2015, **44**, 6184.

54 Z. Wang, X. Qiu, W. Xi, M. Tang, J. Liu, H. Jiang and L. Sun, *Sens. Actuators, B*, 2021, **345**, 130417.

55 Z. Wang, X. Qiu, W. Xi, M. Tang, J. Liu, H. Jiang and L. Sun, *Sens. Actuators, B*, 2023, **376**, 132936.

56 T. Das, S. Das, M. Karmakar, S. Chakraborty, D. Saha and M. Pal, *Sens. Actuators, B*, 2020, **325**, 128765.

57 T. Das, S. Mojumder, S. Chakraborty, D. Saha and M. Pal, *Appl. Surf. Sci.*, 2022, **602**, 154340.

58 Z. Wang, J. Xue, D. Han and F. Gu, *ACS Appl. Mater. Interfaces*, 2015, **7**, 308–317.

59 M. Ali, N. Amrane and N. Tit, *Results Phys.*, 2020, **16**, 102907.